# Parameter Sensitivity Study of Energy Transfer Between Mesoscale Eddies and Wind-Induced Near-Inertial Oscillations

Yu Zhang[1], Jintao Gu[1], Shengli Chen[1*], Jianyu Hu[2], Jinyu Sheng[3], Jiuxing Xing[1]

[1]Institute for Ocean Engineering, Shenzhen International Graduate School, Tsinghua University, Shenzhen, 518055, China

[2]State Key Laboratory of Marine Environmental Science, College of Ocean and Earth Sciences, Xiamen University, Xiamen, 361102, China

[3]Department of Oceanography, Dalhousie University, Halifax, NS B3H 4R2, Canada

*Correspondence to*: Shengli Chen (shenglichen@sz.tsinghua.edu.cn)

**Abstract.** Analyses of current observations and numerical simulations at two moorings in the northern South China Sea reveal the transfer of near-inertial energy between the background currents associated with mesoscale eddies and near-inertial currents (NICs). A series of numerical experiments are conducted to determine important parameters affecting the energy transfer between idealized mesoscale eddies and NICs generated by rotating winds. Speeds of NICs transferred by both cyclonic and anticyclonic mesoscale eddies increase linearly with the wind stress and eddy strength. The transferred NICs in anticyclonic eddies have current amplitudes of about six times larger than in cyclonic eddies. The translation speed of the mesoscale eddy and the wind rotation frequency also affect the conversion of NICs. The energy transfer rate is elevated with the increase of the positive Okubo-Weiss parameter. A simple theoretical analysis is conducted to verify our findings based on numerical results. Analytical solutions confirm the evident asymmetry of the energy transfer between anticyclonic and cyclonic eddies, and demonstrate quantitatively the relationship between the wind stress and the near-inertial energy transferred by mesoscale eddies.

## 1 Introduction

Near-inertial oscillations (NIOs) are very common in the global ocean and they appear as a prominent peak in the spectrum of ocean currents (Garrett, 2001). NIOs contain almost half the total kinetic energy of the internal waves and significantly contribute to the vertical shear in the internal waveband (Ferrari & Wunsch, 2009). When surface winds with high spatiotemporal

29 variations act at the ocean surface, strong NIOs could occur in the ocean surface mixed layer (SML,

30 Chen et al., 2015a; D'Asaro et al. 1995; Pollard & Millard, 1970). At the base of the SML, near-

31 inertial internal waves (NIWs) are generated through the horizontal convergence and divergence

32 of the SML (Gill, 1984). These NIWs are free to radiate to the thermocline and deep waters, and

33 low-mode NIWs with long wavelengths can propagate at least hundreds of kilometers toward the

34 equator from their source regions (Alford, 2003; Jochum et al., 2013; Munk & Wunsch, 1998).

35 NIOs not only affect the energy, momentum, and material transport in the upper ocean, but also

36 play an important role in maintaining diapycnal mixing and global ocean circulation (Chen et al.,

37 2016; Greatbatch, 1984; Price et al., 1986; Wunsch & Ferrari, 2004).

38     Due to the turbulent and inhomogeneous nature of the ocean, the central frequency of NIOs

39 is influenced by the $\beta$ effect and shows a significant blue or red shift induced by the relative

40 vorticity of mesoscale eddies (Chen et al., 2015b; Elipot et al., 2010; Kunze, 1985; Mooers, 1975;

41 Perkins, 1976; Sun et al., 2011). If the magnitude of the gradient in the relative vorticity is larger

42 than the $\beta$ effect (Chelton et al. 2011), mesoscale eddies also modulate the energy distribution and

43 propagation of the near-inertial motions (van Meurs, 1998; Wang et al., 2024). Previous studies of

44 current observations in the northwestern South China Sea (nSCS) demonstrated that the near-

45 inertial energy propagates both upwards and downwards under the influence of the anticyclonic

46 eddies (Chen et al., 2013; Zhai et al., 2007). Using the in situ observations and ray-tracing

47 techniques, Jaimes and Shay (2010) demonstrated that anticyclonic eddies trap the near-inertial

48 kinetic energy which rapidly propagates vertically below the thermocline and even to the deep

49 ocean. Young and Jelloul (1997) suggested that the anticyclonic eddies can improve the vertical

50 propagation rate of the near-inertial energy by deepening the thermocline. Zhai et al. (2005)

51 demonstrated that the wind generated near-inertial kinetic energy is also high in the strong

52 mesoscale motion regions.

53     Mesoscale eddies and NIOs are energetic in the SML (Bühler & McIntyre, 2005; Vanneste,

54 2013; Xie & Vanneste, 2015). Mesoscale eddies not only change the spatial distribution of NIOs,

55 but also exchange the energy with NIOs through the nonlinear interaction (Muller, 1976; Thomas,

56 2012). Based on the observational studies of specific NIO events, Noh and Nam (2020) found that

57 mesoscale eddies can effectively enhance the intensity of NIOs. The energy transfer also occurs

58 between NIOs and low-frequency geostrophic currents through the nonlinear interaction (Liu et

59 al., 2023; Thomas, 2012; Whalen et al., 2020). Jing et al. (2018) demonstrated that the large-scale

60  geostrophic currents of the Gulf Stream affect the distribution of near-inertial energy. Whitt and

61  Thomas (2015) suggested that, in a unidirectional laterally sheared geostrophic flow, a continuous

62  energy transfer occurs between mesoscale eddies and NIOs. In the Kuroshio extension, due to the

63  change of the effective Coriolis frequency caused by the relative vorticity of mesoscale eddies, the

64  energy exchange efficiency between the anticyclonic eddies and NIOs is about twice that between

65  the cyclonic eddies and NIOs (Jing et al., 2017). Based on numerical results in the Icelandic Basin,

66  Barkan et al. (2021) found that a significant energy transfer occurs between NIOs and sub-inertial

67  motions, with the energy transfer rate in winter and summer are about half and a quarter of the

68  local near-inertial wind energy input, respectively. The above and other studies suggested that the

69  energy transfer processes between mesoscale eddies and NIOs should play an important role in the

70  ocean energy cascade (Alford et al., 2016; Ford et al., 2000; McWilliams, 2016; Thomas, 2017).

71  Nevertheless, most of previous studies focused on the energy transfer rate and efficiency. There is

72  a knowledge gap in the amplitude of the near-inertial energy transferred by the mesoscale eddy

73  and the sensitivity of the above-mentioned energy transfer to mesoscale eddies and wind

74  parameters. The main objective of this study is to quantity the energy transfer between the

75  mesoscale eddies and wind-induced NIOs.

76      This paper is structured as follows. Section 2 provides a brief description of observational

77  data and reanalysis used in this study. Section 3 presents the original and modified slab models.

78  Model results for the energy transfer between mesoscale eddies and the NIOs are given in Sect. 4.

79  A series of sensitivity experiments for determining the important factors affecting the energy

80  transfer is presented in Sect. 5. The results of sensitivity experiments are verified through

81  theoretical analysis in Sect. 6. Summary and discussions are given in Sect. 7.

82  **2 Observational and Reanalysis Data**

83      Current observations at two subsurface moorings named S2 and S3 respectively in the nSCS

84  (marked in Fig. 1) are analyzed here. The current observations at these two moorings were made

85  using the Acoustic Doppler Current Profilers (ADCPs). Mooring S2 is located at 117°39.619′ E

86  and 21°37.001′ N. Current observations at this location were made at depth bins from 58 m to 442

87  m from 22 August 2016 to 8 May 2017. At ADCP mooring S2, the vertical sampling interval is

88  16 m and the time internal is 60 minutes. ADCP mooring S3 is located at 117°26.528′ E and

89  21°52.945′ N. Current observations at this mooring were made at depth bins from 37 m to 229 m

90  during the same observational period as at location S2. At mooring S3, the vertical sampling

91  interval is 8 m and the time internal is 30 minutes.

92  Hourly winds at 10 m above the mean sea level in the nSCS were extracted from the European

93  Centre for Medium-Range Weather Forecasts (ECMWF) ERA5 reanalysis. The ERA5 winds from

94  July 2016 to June 2017 with an interval of 1 hour and the horizontal resolution of 0.5° are used to

95  calculate the hourly wind stress to be used as the model forcing.

96  The surface geostrophic currents used in this study were derived from ECMWF, using the sea

97  level grid data inferred from the global marine satellite observations provided by the Copernicus

98  Atmosphere Monitoring Service (C3S). The sea surface height anomaly and geostrophic current

99  data in the nSCS from July 2016 to June 2017 are used here, which have a horizontal resolution of

100  0.25° and a time interval of 24 hours.

101  The mixed layer depth (MLD) for the nSCS was extracted from the 2018 edition of the World

102  Ocean Atlas (WOA2018) (www.ncei.noaa.gov/products/world-ocean-atlas), with a horizontal

103  resolution of 0.25°. The MLD at each location is defined as the depth at which the vertical change

104  of the potential density from the ocean surface is 0.125 (sigma units).

105
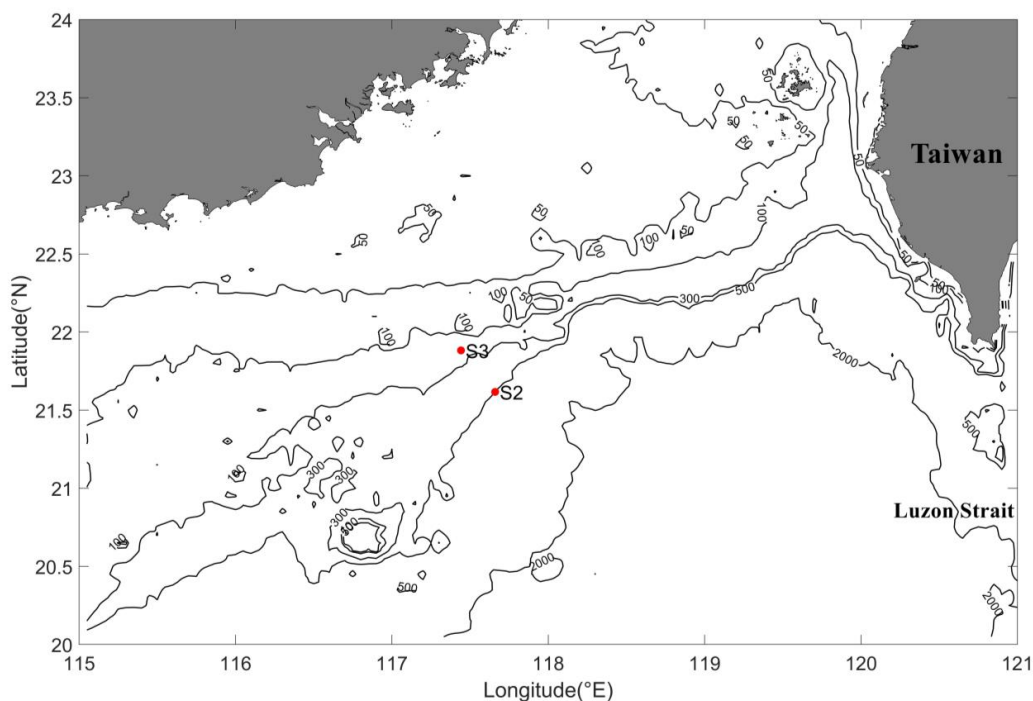


**Figure 1.** Major bathymetric feature of the northern South China Sea. Two red dots represent
locations of two ADCP moorings named S2 and S3. Black contours represent isobaths in meter.

108

## 3 Method

### 3.1 Strain and Vorticity of a Mesoscale Field

The vertical component of the relative vorticity ($\zeta$) has been used to measure the rate of fluid
rotation within a mesoscale eddy, which is defined as

$$\zeta = \frac{\partial V}{\partial x} - \frac{\partial U}{\partial y},$$

(1)

where $U$ and $V$ are zonal (eastward) and meridional (northward) surface geostrophic currents,
respectively.

The normal and shear components of the rate of strain tensor, $S_n$ and $S_s$ are defined as

117
$$S_n = \frac{\partial U}{\partial x} - \frac{\partial V}{\partial y},$$
(2)

118
$$S_s = \frac{\partial V}{\partial x} + \frac{\partial U}{\partial y}.$$
(3)

119 The relative importance of total strain and relative vorticity is diagnosed with the Okubo-
120 Weiss parameter (Okubo 1970):

121
$$OW = S_n^2 + S_s^2 - \zeta^2.$$
(4)

122 In this study, the dependence of the energy transfer between the mesoscale eddy and NICs on
123 the relative vorticity is considered.

**3.2 Modified Slab Model**

125 A simple linear model known as the slab model (Pollard & Millard 1970) was used in
126 simulating NIOs in the SML. Analysis of observed currents in the nSCS (to be discussed in Sect.
127 4) demonstrates that NIOs can also occur in the SML under the nearly steady winds. This suggests
128 the importance of the energy transfer between the background currents and near-inertial currents
129 (NICs). To investigate this energy transfer, the background geostrophic currents $(U, V)$ are added
130 to the original slab model as the modified slab model (Jing et al., 2017; Weller, 1982):

131
$$\begin{cases} \frac{\partial u}{\partial t} + u\frac{\partial U}{\partial x} + v\frac{\partial U}{\partial y} = fv - ru + \frac{\tau_x}{\rho_o\,H_{mix}} \\ \frac{\partial v}{\partial t} + u\frac{\partial V}{\partial x} + v\frac{\partial V}{\partial y} = -fu - rv + \frac{\tau_y}{\rho_o\,H_{mix}} \end{cases},$$
(5)

132 where $(u,v)$ are zonal and meridional currents averaged vertically in the SML, and $H_{mix}$ is the
133 MLD. The damping coefficient $r$ is set to 1/8 days^{-1}, which is used to parameterize the loss of near-
134 inertial energy. In Eq. (5), $f$ is the inertial frequency, and $\rho_o$ is the seawater density set to be 1024
135 kg m^{-3}. Wind stress components $(\tau_x, \tau_y)$ are calculated using 10 m height ERA5 winds with the
136 drag coefficient suggested by Oey et al. (2006).

137 The above modified slab model uses two important assumptions: the Rossby number of the
138 geostrophic currents is assumed to be far less than 1, and the horizontal scale of winds to be much
139 larger than that of mesoscale eddies. By ignoring the background geostrophic currents, the above
140 modified slab model becomes the original slab model, which was used in many previous studies
141 of examining the inertial response in the SML (D'Asaro, 1985; Paduan et al. 1989; Pollard &
142 Millard 1970).

143    The modified slab model in Eq. (5) can be solved numerically using an implicit numerical
144    scheme in time to obtain NICs in the SML:

$$
\begin{cases}
\frac{u^{n+1}-u^n}{\Delta t} + u^{n+1}U_x^{n+1} + v^{n+1}U_y^{n+1} = fv^{n+1} - ru^{n+1} + \frac{\tau_x^{n+1}}{\rho H_{mix}} \\
\frac{v^{n+1}-v^n}{\Delta t} + u^{n+1}V_x^{n+1} + v^{n+1}V_y^{n+1} = -fu^{n+1} - rv^{n+1} + \frac{\tau_y^{n+1}}{\rho H_{mix}}
\end{cases},
\qquad (6)
$$

146    where $\Delta t$ is the time step, which is set to 3600 s in this study, and subscripts $x$ and $y$ in $U$ and $V$
147    represent partial derivatives. The initial value of the NICs is set to 0. In Eq. (6), variables with
148    superscripts $n$ and $n + 1$ represent their values at time $n\Delta t$ and $(n + 1)\Delta t$, respectively.

149    After merging some terms, the numerical scheme of the modified slab model can be written
150    as

$$
\begin{cases}
\frac{u^{n+1}-u^n}{\Delta t} + a_1^{n+1}u^{n+1} + b_1^{n+1}v^{n+1} = c_1^{n+1} \\
\frac{v^{n+1}-v^n}{\Delta t} + a_2^{n+1}u^{n+1} + b_2^{n+1}v^{n+1} = c_2^{n+1}
\end{cases},
\qquad (7)
$$

152    where $a_1 = U_x + r$, $a_2 = V_x + f$, $b_1 = U_y - f$, $b_2 = V_y + r$, $c_1 = \tau_x/\rho H_{mix}$, $c_2 = \tau_y/\rho H_{mix}$.

153    Equation (7) can be written in the following tensor form:

$$
\begin{bmatrix}
a_1^{n+1} + \frac{1}{\Delta t} & b_1^{n+1} \\
a_2^{n+1} & b_2^{n+1} + \frac{1}{\Delta t}
\end{bmatrix}
\begin{Bmatrix} u^{n+1} \\ v^{n+1} \end{Bmatrix}
=
\begin{Bmatrix} \frac{u^n}{\Delta t} + c_1^{n+1} \\ \frac{v^n}{\Delta t} + c_2^{n+1} \end{Bmatrix}.
\qquad (8)
$$

155    The numerical update equations for currents are given as

$$
u^{n+1} = \frac{1+\Delta t b_2^{n+1}}{(1+\Delta t a_1^{n+1})(1+\Delta t b_2^{n+1}) - \Delta t b_1^{n+1} a_2^{n+1}} \left[ \frac{u^n}{\Delta t} + c_1^{n+1} - \frac{\Delta t b_1^{n+1}}{1+\Delta t b_2^{n+1}} \left( \frac{v^n}{\Delta t} + c_2^{n+1} \right) \right], \quad (9)
$$

$$
v^{n+1} = \frac{1+\Delta t a_1^{n+1}}{(1+\Delta t a_1^{n+1})(1+\Delta t b_2^{n+1}) - \Delta t b_1^{n+1} a_2^{n+1}} \left[ \frac{u^n}{\Delta t} + c_1^{n+1} - \frac{\Delta t a_2^{n+1}}{1+\Delta t a_1^{n+1}} \left( \frac{v^n}{\Delta t} + c_2^{n+1} \right) \right]. \quad (10)
$$

158    **3.3 Analysis of NICs**

159    The observed zonal and meridional currents at 58.3 m below the sea surface at location S2
160    and at 37.7 m at location S3 (marked in Fig. 1) in the nSCS are analyzed to estimate the near-
161    inertial kinetic energy in the SML. The observed NICs are obtained by using a band-pass filter
162    with a frequency band of $0.85f$-$1.15f$.

163    The surface geostrophic currents described in Sect. 2 are specified in the modified slab model,

164    based on the assumption that the geostrophic currents are vertically uniform in the SML during

165    the study period. The simulated currents by the original and modified slab models are band-passed

166    with the frequency band of $0.85f$-$1.15f$ and are further smoothed using a running window of two

167    inertial periods to obtain the simulated NICs.

168    To quantitatively assess performances of the original and modified slab models, the

169    correlation analysis and root mean square error (RMSE) analysis between the original slab model,

170    the modified slab model and observations respectively are made.

171    **4 Results**

172    **4.1 Observed NICs**

173    Time series of observed NICs at the top depth bins (58.3 m at S2 and 37.7 m at S3) of two

174    subsurface ADCP moorings (known as $\vec{u}_{S2}^{top}$ and $\vec{u}_{S3}^{top}$) are shown in black lines in Fig. 2 during

175    the observational period from day 234 (22 August 2016) to day 492 (7 May 2017) with respect to

176    1 January 2016. Intense NICs were generated and lasted for about 11 days from day 293 to day

177    304 under the largest wind forcing (~1.6 N m$^{-2}$) on day 293 (Fig. 2e and 2f). The largest speed of

178    NICs was ~0.30 m s$^{-1}$ on day 295 at the top depth bin at mooring S2 (Fig. 2a) and ~0.37 m s$^{-1}$ on

179    day 296 at the top depth bin at mooring S3 (Fig. 2b). Some NICs were also excited on other days

180    when the winds were relatively weak and nearly steady.
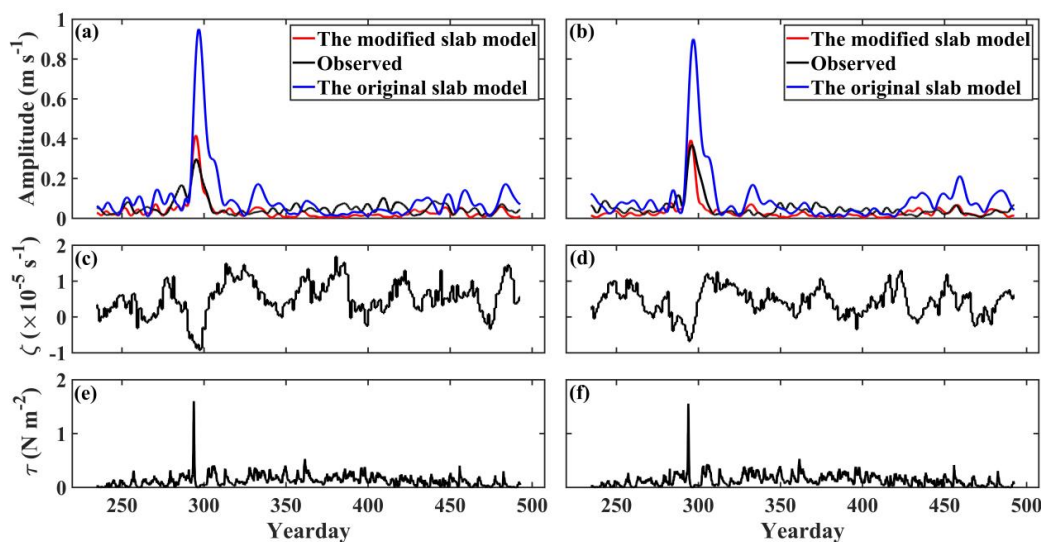
**Figure 2.** Speeds (m s$^{-1}$) of observed (black line) and simulated NICs at the top depth bins of ADCP observations at moorings (a) S2 and (b) S3. Red and blue lines denote model results produced by the modified slab and original slab models respectively. Time series of relative vorticity of the surface geostrophic currents at moorings (c) S2 and (d) S3, and time series of wind stress at moorings (e) S2 and (f) S3. Yearday is the day relative to 00:00:00 (GMT) on 1 January 2016.

Observed NICs at other depth bins of these two ADCP moorings reveal that the intense NICs occurred on days 293-304 at depths between 60 m and 200 m at mooring S2 (not shown) and these NICs were originated from the SML. At mooring S3, similar intense NICs occurred at depths between 40 m and 180 m on days 280-305 (not shown), and these NIC were also originated from the SML. On days 306-318, in comparison, moderate NICs occurred in the lower layer between 150 m and 310 m at these two moorings.

It should be noted that the current observations ($\vec{u}_{S2}^{top}$ and $\vec{u}_{S3}^{top}$) at the top bins of the two ADCP moorings are in the lower part of the SML or below the SML during the observational period. Based on WOA2018, the climatological monthly mean MLD at the two ADCP moorings is the thinnest and ~20 m in August and increases to the maximum value of ~90 m in January. The MLD decreases from ~56 m in February to ~37 m in May and is about 25 m in June and July. This suggests that the observed NICs at the top depth bin (58.3 m) of S2 were made in the lower part of the SML in December and January (days 335-396), but below the SML on the other days of the observational period (Fig. 2a). By comparison, the observed NICs at the top depth bin (37.7 m) of

9

203 S3 were made in the middle of the SML in December and January (days 335-396), and in the lower

204 part of the SML in October and November (days 274-334) and February-May (days 397-492).

205    The relative vorticity estimated from the surface geostrophic currents was negative at the two

206 moorings on days 290-300 (Fig. 2c and 2d), with the maximum negative values of about $-0.92 \times 10^{-5}$ s$^{-1}$

207 at mooring S2 and about $-0.68 \times 10^{-5}$ s$^{-1}$ at mooring S3. The negative values of the relative

208 vorticity during this period resulted from the westward propagation of an anticyclonic eddy. As

209 shown in Fig. 3a and 3f, on day 295, moorings S2 and S3 were located over the area between a

210 relatively strong cyclonic eddy to the southwest and two separate weak cyclonic eddies to the east

211 and south. The anticyclonic eddy moved westward and passed mooring S2 before day 316 (Fig.

212 3b and 3g). On day 316, the relative vorticity was low and positive of about $1.23 \times 10^{-5}$ s$^{-1}$ at

213 mooring S2 and $0.83 \times 10^{-5}$ s$^{-1}$ at mooring S3 respectively. On days 350-450, an anticyclonic eddy

214 moved westward and passed through these two moorings S2 and S3, and there was a week cyclonic

215 eddy close to the two moorings on day 435 (Fig. 3c, 3d, 3h, and 3i). The relative vorticity was

216 relatively strong and positive during this period, with the maximum positive values of about

217 $1.68 \times 10^{-5}$ s$^{-1}$ on day 380 at mooring S2 and $1.29 \times 10^{-5}$ s$^{-1}$ on day 423 at mooring S3 respectively.

218 Between days 451-492, there is a week anticyclonic eddy close to the moorings S2 and S3 and the

219 two moorings are located at the edge of the anticyclonic eddy on day 452 (Fig. 3e and 3j).

220
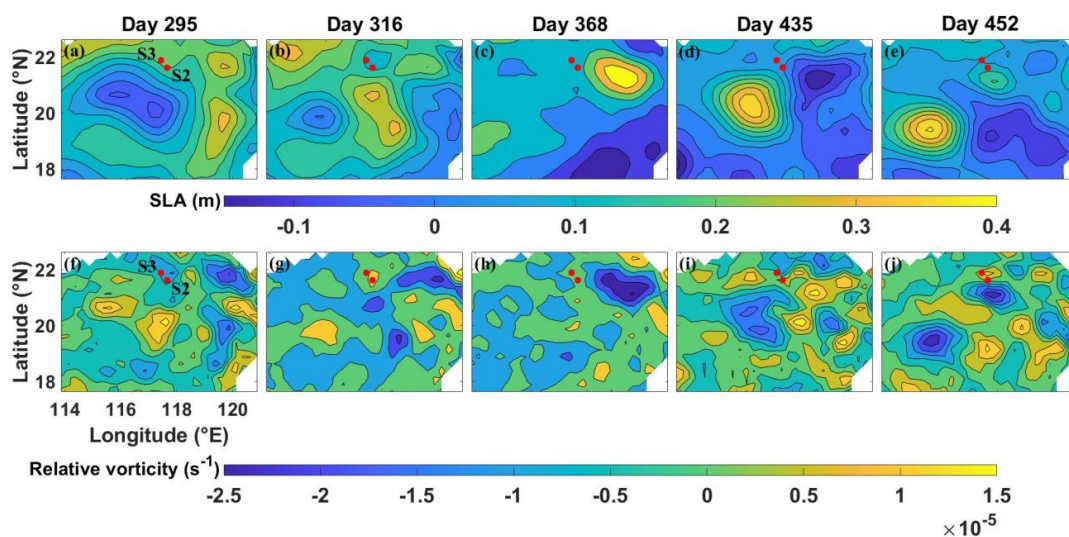


222 **Figure 3.** Spatial distributions of sea surface level anomaly (SLA) on day 295 (a), day 316 (b),
223 day 368 (c), day 435 (d) and day 452 (e). Spatial distributions of the relative vorticity on day 295

224 (f), day 316 (g), day 368 (h), day 435 (i) and day 452 (j). Two red dots mark locations of two
225 ADCP moorings S2 and S3.

**4.2 Simulated NICs**

227     Numerical simulations are made using the original and modified slab models to examine
228 whether the energy exchange occurs between the mesoscale eddy and NICs in the SML at
229 moorings S2 and S3. Both the original and modified slab models assume that the NICs in the SML
230 is vertically uniform and use the damping coefficient $r$ set to a relatively small value of 1/8 day$^{-1}$.
231 Both the models are forced by time series of wind stress shown in Fig. 2e and 2f.

232     The simulated NICs produced by the original slab model at the top bins of two ADCP
233 moorings are shown by the blue lines in Fig. 2a and 2b. The simulated NICs by the original slab
234 model are large and about 0.95 m s$^{-1}$ (0.90 m s$^{-1}$) at mooring S2 (S3) on day 296 and relatively
235 weak on days 350-430. In comparison with the observed NICs, the original slab model has large
236 deficiency of overpredicting significantly the observed large NICs on days 285-300 at the two
237 stations and also overpredicting moderately the observed NICs on other days of the observational
238 period. It should be noted that the results of both the original and modified slab models using three
239 different damping coefficients ($r$ = 1/5 day$^{-1}$, 1/6 day$^{-1}$ and 1/7 day$^{-1}$) and annual mean MLD at
240 two stations (~45 m) are highly similar with the model results using $r$ = 1/8 day$^{-1}$ and monthly
241 mean MLD shown in Fig. 2a and 2b.

242     In comparison with the original slab model results, the modified slab model generates much
243 smaller NICs than the original slab model on days 280-305 (red lines in Fig. 2a and 2b), with the
244 maximum value of about 0.42 m s$^{-1}$ at mooring S2 and about 0.39 m s$^{-1}$ at mooring S3 on day 295.
245 In comparison with the observed NICs at the two moorings, the modified slab model performs
246 significantly better than the original slab model on days 250-325 and days 451-492, indicating the
247 importance of the energy exchange between the background mesoscale eddies and NICs. On days
248 350-450, the relative vorticity of the background currents is positive, which results in the simulated
249 NICs produced by the modified slab model to be slightly weaker than the observed NICs at these
250 two moorings. As mentioned in Sect. 4.1, the top depth bins of the ADCP observations at the two
251 moorings were in the lower part of the SML or below the SML during the observational period,
252 which explains partially the differences between observed and simulated NICs by the modified
253 slab model shown in Fig. 2a and 2b. Differences between the observed and simulated NICs can

254  also partially be explained by the assumption of vertically uniform geostrophic currents in the

255  SML and exclusion of baroclinic dynamics.

256      The above analysis based on results shown in Fig. 2 suggests that, overall, the simulated NICs

257  produced by the modified slab model agree with the observed NICs significantly better than the

258  original slab model at two moorings S2 and S3. This indicates the occurrence of the near-inertial

259  energy transfer induced by the interaction between mesoscale eddies and NICs in the SML during

260  the observational period.

261       To quantify the model performance, we use the correlation coefficient (R) and the root mean

262  square error (RMSE) based on the time series of observed and simulated NICs shown in Fig. 2a

263  and 2b. The modified slab model has a higher correlation coefficient (R = ~0.81) and smaller root

264  mean square error (RMSE = ~0.04 m s$^{-1}$) than the original slab model (R = ~0.70 and RMSE =

265  ~0.12 m s$^{-1}$) at mooring S2. At mooring S3, the R value between the observed NICs and results of

266  the modified slab model is ~0.84, and RMSE is ~0.03 m s$^{-1}$. For the original slab model at location

267  S3, the R value is ~0.85, and RMSE is ~0.10 m s$^{-1}$. These statistical indices suggest that the

268  modified slab model performs better than the original slab model, especially in reproducing the

269  amplitude of the observed NICs. This also suggests the energy transfer between mesoscale eddies

270  and NICs may be a non-negligible process in the energy cascade across different scales in the

271  global ocean.

272

273  **Table 1.** Correlation coefficients (*R*) and RMSEs between the simulation results of the modified
274  and original slab models and observations for the observational period, respectively.

| Mooring | Correlation coefficient (*R*) | | RMSE (m s$^{-1}$) | |
|---|---|---|---|---|
| | Original slab model | Modified slab model | Original slab model | Modified slab model |
| S2 | 0.70 | 0.81 | 0.12 | 0.04 |
| S3 | 0.85 | 0.84 | 0.10 | 0.03 |

275  **5 Sensitivity Study**

276      A series of numerical experiments (in total 196) are conducted using the original and modified

277  slab models to examine sensitivity of model results to the wind speed, the wind rotation frequency,

278  the translational speed of the mesoscale eddy, and the strength of the mesoscale eddy. Both the

279  cyclonic and anticyclonic eddies with an idealized eddy structure are used for simplicity. Results

280    of the original and modified slab models are both band-pass ($0.60f$-$1.40f$) filtered to get broad

281    NICs signals and then smoothed using a running window to obtain the near-inertial velocity in the

282    SML.

### 5.1 Idealized Mesoscale Eddy Structure

284    Based on the composite analysis of satellite altimetry and Argo float data, Zhang et al. (2013)

285    suggested a universal structure of mesoscale eddies in the global ocean. Their universal structure

286    of mesoscale eddies is used in our experiments.

287    The normalized structure $\tilde{P}(\tilde{r}, z)$ of the pressure anomaly in the universal mesoscale eddy

288    used in this study is decomposed into a radial function $R(\tilde{r})$ and a vertical function $H(z)$:

$$\tilde{P}(\tilde{r}, z) = R(\tilde{r})\,H(z), \tag{11}$$

$$R(\tilde{r}) = \left(1 - \frac{\tilde{r}^2}{2}\right) e^{-\frac{\tilde{r}^2}{2}}, \tag{12}$$

$$H(z_s) = H_0 \sin(kz_s + \theta_0) + H_{ave}, \tag{13}$$

$$\tilde{r} = \frac{r}{R_0}, \tag{14}$$

$$z_s = \int_0^z \left(\frac{N}{f}\right) dz, \tag{15}$$

294    where $r$ is the radial distance to the eddy center, $R_0$ is the radius of the mesoscale eddy, N is the

295    buoyancy frequency, $H_0$, $k$, $\theta_0$ and $H_{ave}$ are undetermined coefficients, e.g. in this study, $H_0 =$

296    $2/3$，$H_{ave} = 2/3$，$N = 10^{-3}\ (1/s)$，$k = \pi/18000$，$f = 5 \times 10^{-5}\ (rad/s)$ and $\theta_0 = \pi/6$.

297    The vertical structure function $H(z)$ defined above is similar with the structural diagram in Zhang

298    et al. (2013).

299    The structure function for the idealized mesoscale eddy in the Cartesian coordinate system

300    can be written as

$$\tilde{P}(x, y, z) = \left(1 - \frac{x^2 + y^2}{2R_0^2}\right) \cdot e^{-\frac{x^2 + y^2}{2R_0^2}} \cdot \left[\frac{2}{3} \cdot \sin\left(\frac{\pi}{900} \cdot z + \frac{\pi}{6}\right) + \frac{2}{3}\right], \tag{16}$$

302    with the origin of the coordinate to be the eddy center at the sea surface.

303    Using the pressure anomaly suggested by Wei et al. (2017), the equation for the pressure field

304    based on the different strength of mesoscale eddies can be given as

$$P(x, y, z) = P_0 \cdot \tilde{P}(x, y, z) + \bar{P}(z), \tag{17}$$

$$P_0 = g \cdot \rho_0 \cdot SLA_c, \tag{18}$$

307 where $P_0$ is the strength of mesoscale eddies，$\rho_0$ is the reference density of seawater taken as

308 1024 kg/m³ , $g$ is the gravitational acceleration set to be 9.8 m/s², $SLA_c$ is the sea surface level

309 anomaly (SLA) of the eddy center where the anticyclone eddies are specified as negative values

310 and the cyclonic eddies are positive values, and the average pressure field is denoted by $\bar{P}$. As only

311 mesoscale eddy signals are added to the ocean in this study, $\bar{P}$ is a function of the vertical direction

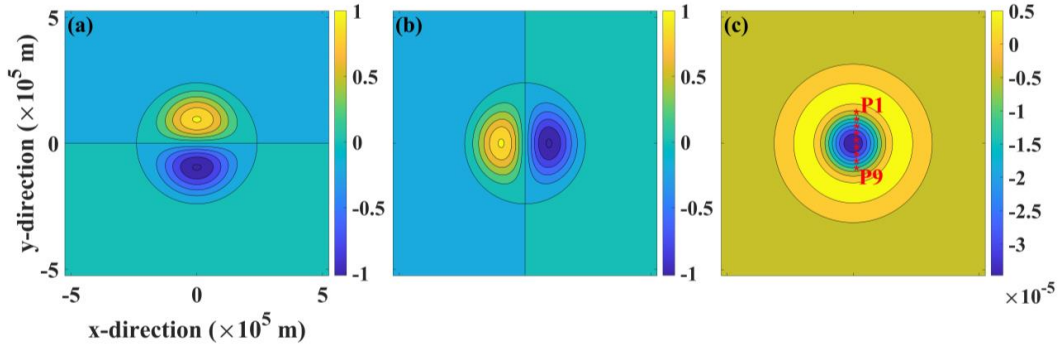312 that is homogeneous in the horizontal direction.

313     Using the geostrophic balance, the zonal and meridional components of the geostrophic

314 velocity at the ocean surface are given as

$$u = -\frac{1}{\rho_0 f}\frac{\partial P}{\partial y} = -\frac{P_0}{\rho_0 f}\left[\frac{y^3 + yx^2 - 4yR_0^2}{2R_0^4}\right] e^{-\frac{x^2+y^2}{2R_0^2}}, \tag{19}$$

$$v = \frac{1}{\rho_0 f}\frac{\partial P}{\partial x} = \frac{P_0}{\rho_0 f}\left[\frac{x^3 + xy^2 - 4xR_0^2}{2R_0^4}\right] e^{-\frac{x^2+y^2}{2R_0^2}}. \tag{20}$$

317     In this study, the cyclonic and anticyclonic eddies are set to have the same strength with the

318 opposite relative vorticity. Figure 4 shows currents and relative vorticity at the sea surface for an

319 idealized anticyclonic eddy with the radius of 120 km, $R_0$ to be 120 kilometers, and $P_0$ of

320 6400 kg/m $\cdot$ s² (i.e., $SLA_c$ is equal to 0.64 m). Based on Eq. (18), the mesoscale eddy strength $P_0$

321 is a positive proportional function of the $SLA_c$ under the constant seawater density and

322 gravitational acceleration. The strength of the mesoscale eddy can be characterized by the absolute

323 values of the $SLA_c$ ($|SLA_c|$).

324     To examine model results inside the eddy, nine fixed locations in space named P1-P9 along

325 the y-axis (marked in Fig. 4c) are selected. The zonal and meridional components of currents for

326 an anticyclonic eddy increase from the center to the edge of the eddy, and then gradually decrease

327 outside the anticyclonic eddy (Fig. 4a and 4b). The relative vorticity is largest at the eddy center

328 and then reduces gradually from the center to the edge of the eddy (Fig. 4c). The idealized eddy

329 has a velocity reversal from the eddy center outward, which forms a circular positive (negative)

330 vorticity around the periphery of the idealized anticyclonic (cyclonic) eddy in the Northern

331 Hemisphere (Zhang et.al 2013).

**Figure 4.** Distributions of (a) zonal ($u$) and (b) meridional ($v$) components (m s$^{-1}$) of currents and (c) relative vorticity (s$^{-1}$) for an idealized anticyclonic eddy with of radius of 120 km. Model results at nine fixed locations (P1-P9) denoted by red asterisks along the y-axis in (c) are examined.

Jing et al. (2017) proposed a method to calculate the efficiency of energy transfer from background mesoscale eddies to wind-induced NICs. In this study, we use the differences in the average speeds of NICs between the modified and original model (NICs_U$_{AE}$ and NICs_U$_{CE}$) as the proxies for the near-inertial energy generated in the mesoscale eddies by the interaction between mesoscale eddies and NICs:

$$NICs\_U_{AE} = NICs\_U_{AE}^{Modified} - NICs\_U_{AE}^{Original}, \qquad (21)$$

$$NICs\_U_{CE} = NICs\_U_{CE}^{Modified} - NICs\_U_{CE}^{Original}, \qquad (22)$$

where $NICs\_U_{AE}^{Modified}$ ($NICs\_U_{AE}^{Original}$) and $NICs\_U_{CE}^{Modified}$ ($NICs\_U_{CE}^{Original}$) are the averaged speeds of NICs based on results produced by the modified (original) slab model in the anticyclonic eddies and cyclonic eddies over the same time period, respectively. It should be noted that the simulated NICs by the original slab model represent the near-inertial energy generated directly by the wind forcing. Therefore, after removing the generation of wind-induced NICs, the differences $NICs\_U_{AE}$ and $NICs\_U_{CE}$ represent the amplitudes of NICs transferred by interactions between mesoscale eddies and NICs in the anticyclonic eddies and the cyclonic eddies respectively.

To quantify differences in the NICs transferred by background currents between the anticyclonic and cyclonic eddies, we introduce a simple parameter $\alpha$, defined as

$$\alpha = \frac{NICs\_U_{AE}}{NICs\_U_{CE}}. \qquad (23)$$

15

354 If $\alpha$ is larger than 1, it means that the anticyclonic eddy can transfer more NICs than the cyclonic

355 eddy with the same strength.

**5.2 Effect of Wind Speeds**

357 The wind speed affects the energy input from the wind to the SML, and therefore influences

358 interaction between mesoscale eddies and NICs. To facilitate theoretical analysis and generate a

359 reasonable magnitude of the NICs speeds, we conduct the numerical experiments using

360 cyclonically rotating winds and anticyclonically rotating and in the Northern Hemisphere with the

361 constant wind speed (A). The wind stress $\tau$ used in our sensitivity study takes a form as follows

$$\tau_x(t) + i\,\tau_y(t) = A\,e^{iBt}, \tag{24}$$

363 where $\tau_x(t)$ and $\tau_y(t)$ are time-dependent zonal and meridional components of wind stress, and

364 $B$ is the wind rotation frequency. Positive wind rotation frequencies represent cyclonically

365 rotating winds and negative wind rotation frequencies indicate anticyclonically rotating winds.

366 Five numerical experiments (ExpA1-5) are conducted with the background idealized

367 mesoscale eddy moving westward with a translational speed of 8 cm s$^{-1}$. The $|SLA_c|$ of both

368 anticyclonic and cyclonic eddies are set to 0.64 m in these five experiments. The speeds (A) of

369 time-varying winds in these five experiments are set to 5 m s$^{-1}$, 10 m s$^{-1}$, 13 m s$^{-1}$, 15 m s$^{-1}$, and 20

370 m s$^{-1}$ respectively, corresponding to wind stress amplitudes of 0.038 N m$^{-2}$, 0.150 N m$^{-2}$, 0.282 N

371 m$^{-2}$, 0.412 N m$^{-2}$, and 0.876 N m$^{-2}$ respectively. The wind forcing rotates cyclonically at the inertial

372 frequency $f$.

373 For a cyclonic eddy with $|SLA_c| = 0.64$ m, the sum of averaged speeds of NICs converted

374 from this cyclonic eddy at the above-mentioned nine locations ($\sum \text{NICs\_U}_{CE}$) are about 0.009 m s$^{-1}$

375 and 0.209 m s$^{-1}$ for cyclonic wind speeds of 5 m s$^{-1}$ (i.e. 0.038 N m$^{-2}$) and 20 m s$^{-1}$ (i.e. 0.876 N

376 m$^{-2}$) respectively (Fig. 5a). This suggests that, within the cyclonic eddy, the $\sum \text{NICs\_U}_{CE}$ increases

377 23 times if the cyclonic wind stress increases 23 times, which is consistent with the conclusion

378 based on the analytical solution in Sect. 6.

379 In an anticyclonic eddy with the same strength of $|SLA_c| = 0.64$ m, the sum of averaged

380 speeds of NICs transferred from this anticyclonic eddy at the nine locations ($\sum \text{NICs\_U}_{AE}$) also

381 increases with the wind speeds. The $\sum \text{NICs\_U}_{AE}$ values are about 0.019 m s$^{-1}$ and 0.437 m s$^{-1}$ for

382 the cyclonic wind speeds of 5 m s$^{-1}$ (corresponding to 0.038 N m$^{-2}$) and 20 m s$^{-1}$ (corresponding to

383    0.876 N m$^{-2}$) respectively (Fig. 5a). This indicates that the averaged speeds of NICs generated in

384    anticyclonic eddies by the interaction between background anticyclonic eddies and NICs also

385    increase 23 times if the cyclonic wind stress increases 23 times. But the NICs are stronger in the

386    anticyclonic eddy than in the cyclonic eddy under the same wind conditions.

387
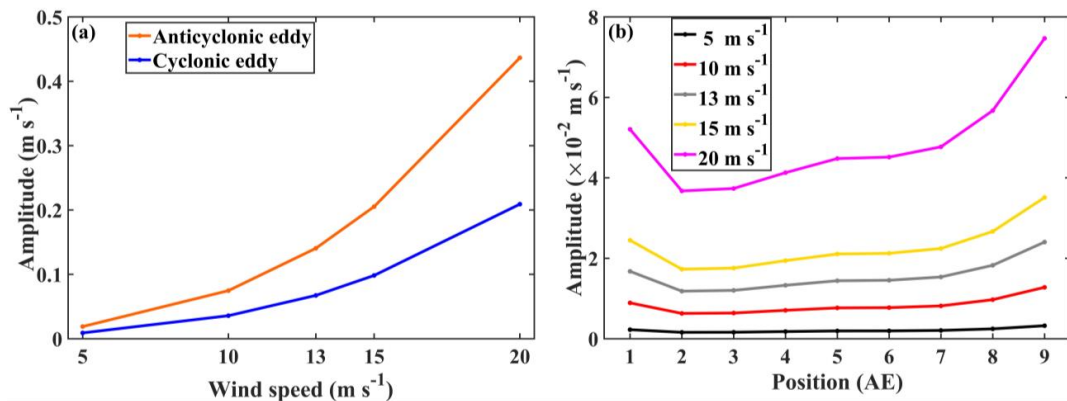


388

389    **Figure 5.** (a) Sum of averaged speeds of transferred NICs at 9 fixed locations P1-P9 as a function
390    of the wind speeds in the anticyclonic eddy (orange line) and cyclonic eddy (blue line), respectively.
391    (b) Averaged speeds of transferred NICs as a function of the wind speeds in the anticyclonic eddy.
392    The black, red, gray, yellow and purple line indicate respectively the wind speed of 5 m s$^{-1}$ (ExpA1),
393    10 m s$^{-1}$ (ExpA2), 13 m s$^{-1}$ (ExpA3), 15 m s$^{-1}$ (ExpA4) and 20 m s$^{-1}$ (ExpA5). Numbers on the
394    horizontal axis in (b) denote nine fixed locations P1 to P9. The wind rotates cyclonically at the
395    inertial frequency. Mesoscale eddies move westward at the translational speed of 8 cm s$^{-1}$ and
396    $|SLA_c| = 0.64$ m.

397

398    It should be noted that, however, the transferred near-inertial energy varies with the actual

399    locations within the mesoscale eddy. We take the example of anticyclonic eddies to illustrate this

400    issue. In anticyclonic eddies, the difference between nine locations P1-P9 is large (Fig. 5b). The

401    amplitude shows a distribution characterized by small values at the eddy center and relatively large

402    values at the eddy edge, and this distribution characteristic is more obvious with the increase of

403    the wind speed. When the wind speed is relatively small, the difference of the energy generation

404    induced by the Okubo-Weiss parameter is not significant. With the increase of the wind energy

405    input, the larger absolute value of the positive Okubo-Weiss parameter gradually has the decisive

406    function in the energy transfer. Therefore, it makes the anticyclonic eddy exhibit superior energy

407    conversion characteristics at the eddy edge, which is consistent with the conclusion based on the

408    energy transfer rate (Fig. 10).

409    The $\alpha$ values (Eq. (23)) are about 2.08 based on the sum of averaged speeds of NICs at the

410    nine locations in the five different wind speeds. This indicates that the anticyclonic eddy is more

411    efficient than the cyclonic eddy in transferring the kinetic energy to NICs (Fig. 5a). The difference

412    in the near-inertial energy transfer efficiency between anticyclonic and cyclonic eddies is not

413    affected very much by magnitudes of wind speeds.

### 5.3 Effect of Wind Rotation Frequencies

415    The rotation frequency of the winds can affect the generation of the NICs and thus the energy

416    transfer between the mesoscale eddy and NICs, therefore six numerical experiments using different

417    wind rotation frequencies (-1.5$f$, -1.25$f$, -1.1$f$, -0.9$f$, -0.75$f$, -0.5$f$, -0.25$f$, 0.25$f$, 0.5$f$, 0.75$f$,

418    $f$, 1.25$f$ and 1.5$f$, where $f$ is the inertial frequency), denoted as ExpB1-13, are conducted.

419    Positive wind rotation frequencies correspond to cyclonically rotating winds, and negative wind

420    rotation frequencies are for anticyclonically rotating winds. In these thirteen experiments, the

421    mesoscale eddy moves westward at the speed of 8 cm s$^{-1}$ and $|SLA_c|$ = 0.64 m. The winds rotate

422    at different frequencies and the wind speed is set to 13 m s$^{-1}$.

423    Figure 6 shows the sum of averaged speeds of the transferred NICs at the nine locations as

424    function of the wind rotation frequency for the cyclonic and anticyclonic eddies. Under

425    cyclonically rotating and anticyclonically rotating wind conditions, there is bidirectional energy

426    transfer between mesoscale eddies and NICs. The closer the absolute value of the wind rotation

427    frequency to $f$, the stronger the energy transfer between mesoscale eddies and NICs.

428    For cyclonic eddies, the sum of averaged speeds of NICs ($\sum$NICs_U$_{CE}$) is sensitive to the

429    wind rotation frequency. The $\sum$NICs_U$_{CE}$ values are less than zero when the winds rotate

430    cyclonically at the frequencies of 0.25$f$, 0.75$f$ and 1.25$f$ (Fig. 6b) and the winds rotate

431    anticyclonically at the frequencies of -1.1$f$, -0.9$f$ and -0.75$f$ (Fig. 6a), indicating that direction of

432    the energy transfer is from the NICs to the cyclonic eddies. The amplitudes of the energy

433    transferred from NICs to cyclonic eddies under anticyclonically rotating wind conditions are larger

434    than those transferred under cyclonically rotating wind conditions. The addition of mesoscale

435    eddies has a damping effect for NICs, leading to the negative energy transfer that aligns with the

436    observed results (Fig. 2). When the direction of the energy transfer is positive, the $\sum$NICs_U$_{CE}$ has

437　　a maximum value of about 0.635 m s$^{-1}$ when the winds rotate anticyclonically at the frequency of

438　　-1.25$f$.

439　　　　For anticyclonic eddies, the sum of averaged speeds of NICs ($\sum$ NICs_U$_{AE}$) also varies with

440　　the wind rotating frequency. When the winds rotate anticyclonically at frequencies of -1.5$f$, -1.25$f$,

441　　-1.1$f$ and -0.9$f$, the direction of the energy transfer is from NICs to anticyclonic eddies (Fig. 6a).

442　　The negative energy transfer is strongest at the frequency of -1.1$f$. The $\sum$ NICs_U$_{AE}$ values are all

443　　positive under cyclonically rotating winds, which represent the energy transfer from the

444　　anticyclonic eddies to NICs (Fig. 6b). The $\sum$ NICs_U$_{AE}$ values for the anticyclonic eddies increases

445　　from the value of ~0.002 m s$^{-1}$ at the wind rotating frequency of 0.25$f$ to the maximum value of

446　　~0.162 m s$^{-1}$ at the wind rotating frequency of 0.75$f$. The $\sum$ NICs_U$_{AE}$ values are larger than the

447　　$\sum$ NICs_U$_{CE}$ values under the same positive wind rotation frequency. The closer the rotational

448　　frequency of the cyclonic winds is to the inertial frequency, the greater the difference in near-

449　　inertial energy conversion induced by anticyclonic eddies and cyclonic eddies.

450
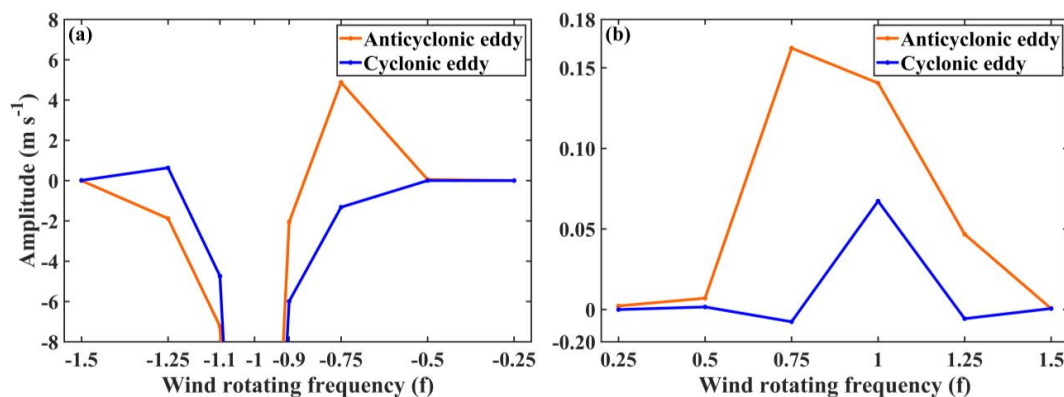
451


452　**Figure 6.** Sum of averaged speeds of transferred NICs at 9 fixed locations P1-P9 as a function of
453　rotation frequencies of (a) anticyclonically rotating winds and (b) cyclonically rotating winds. The
454　orange and blue line indicate respectively the anticyclonic eddy and cyclonic eddy. The wind
455　rotation frequencies are normalized by the inertial frequency $f$.

456　**5.4 Effect of Eddy Translational Speeds**

457　　　　The translational speed of a background mesoscale eddy defines the forcing duration of winds

458　　and thus the energy input to NICs in the ocean SML. Based on the observations of mesoscale

459    eddies in the nSCS, nine numerical experiments (ExpC1-9) using different translational speeds of

460    mesoscale eddies (4 cm s$^{-1}$, 5 cm s$^{-1}$, 6 cm s$^{-1}$, 7 cm s$^{-1}$, 8 cm s$^{-1}$, 9 cm s$^{-1}$, 10 cm s$^{-1}$, 11 cm s$^{-1}$, and

461    12 cm s$^{-1}$) are conducted. In these nine experiments, the speed of cyclonically rotating winds at the

462    inertial frequency is set to 13 m s$^{-1}$. The mesoscale eddy moves westward and $|SLA_c| = 0.64$ m.

463        For the anticyclonic eddy with $|SLA_c| = 0.64$ m, the sum of average speeds of the converted

464    NICs at the nine locations ($\sum$ NICs_U$_{AE}$) increases from about 0.133 m s$^{-1}$ to 0.148 m s$^{-1}$ as the

465    translational speeds increase from 4 cm s$^{-1}$ to 12 cm s$^{-1}$ (Fig. 7a). The increase of the translational

466    speed enhances the total kinetic energy of mesoscale eddies, which can provide a larger energy

467    source and be more beneficial for the conversion of NICs. It should be noted that the change in the

468    eddy kinetic energy caused by the different translational speeds is relatively small in comparison

469    with the total eddy energy determined by the mesoscale eddy strength. Therefore, the change in

470    the amplitude of the transferred NICs is relatively small.

471        For a cyclonic eddy with $|SLA_c| = 0.64$ m, the sum of average speeds of the transferred NICs

472    at the nine locations ($\sum$ NICs_U$_{CE}$) range from 0.066 m s$^{-1}$ to 0.069 m s$^{-1}$ and are not sensitive to

473    the translational speeds (Fig. 7a). Same as in the anticyclonic eddy case, more total kinetic energy

474    is available for generating NICs within the cyclonic eddy with the same structure but with the

475    faster translational speeds. Different from the anticyclonic eddy case, however, the anticyclonic

476    eddy is not conducive to the energy transfer to NICs naturally. Therefore, the slightly larger energy

477    source caused by the increase of the translational speeds has little influence on the total amount of

478    kinetic energy transferred from the cyclonic eddy to NICs.

479
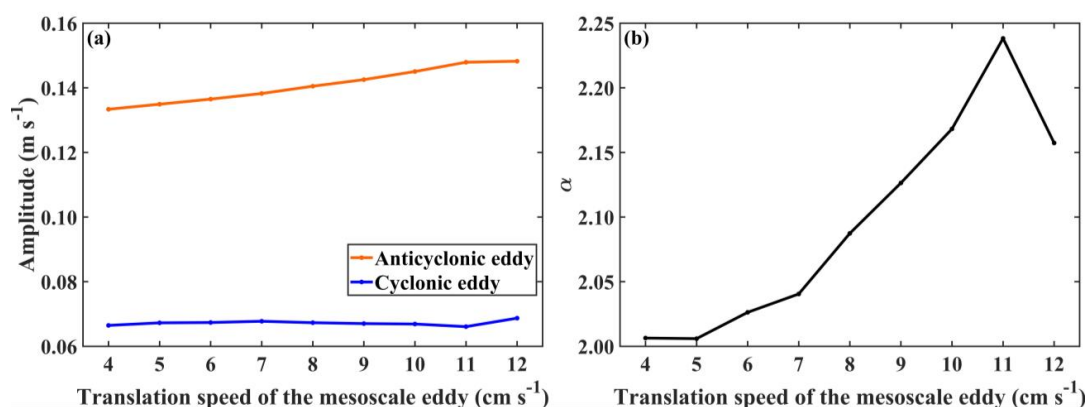


480

481    **Figure 7.** (a) Sum of averaged speeds of transferred NICs at 9 fixed locations P1-P9 as a function
482    of the eddy translational speed in the anticyclonic eddy (orange line) and cyclonic eddy (blue line),
483    respectively. (b) The $\alpha$ value as a function of the eddy translational speed. The speed of the
484    cyclonic wind is 13 m s$^{-1}$, and the wind rotates at the inertial frequency. Mesoscale eddies move
485    westward and $|SLA_c|$ = 0.64 m.

486

487        The $\alpha$ value has a maximum value of ~2.24 occurring at the eddy translational speeds of 11

488    cm s$^{-1}$ (Fig. 7b). This means that the anticyclonic eddy transfers much more near-inertial energy

489    than the cyclonic eddy does, particular at the translational speed of 11 cm s$^{-1}$. After exceeding the

490    translational speed of 11 cm s$^{-1}$, the $\alpha$ values decrease with the increase of the eddy translational

491    speeds. The $\alpha$ value is ~2.16 at the translational speed of 12 cm s$^{-1}$.

492        A natural question raises whether the variations of $\alpha$ values within the mesoscale eddy are

493    affected by the strength of anticyclonic eddies. To address this issue, we consider the sum of

494    averaged speeds of NICs at nine locations for mesoscale eddies and the $\alpha$ values with different

495    strengths and translational speeds (Fig. 8). We consider the case with the cyclonically rotating

496    wind speed of 13 m s$^{-1}$ at the inertial frequency. For mesoscale eddies with larger $|SLA_c|$ values,

497    the $\alpha$ values are relatively less sensitive to the translational speed. For mesoscale eddies with

498    different $|SLA_c|$ values, the $\alpha$ values all have the maximum values with the translational speeds of

499    11 cm s$^{-1}$. The $\alpha$ value decreases with the elevated translational speed when the eddy translational

500    speed is larger than 11 cm s$^{-1}$.

501
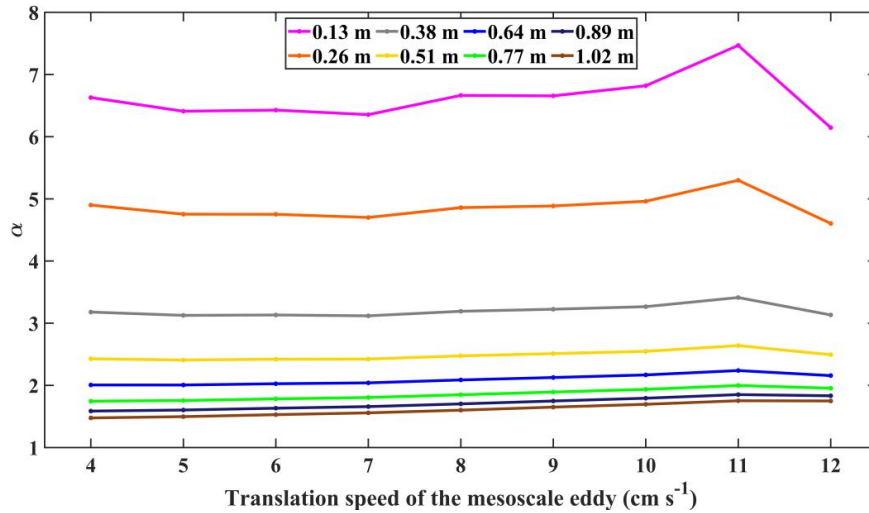
**Figure 8.** The $\alpha$ values at 9 fixed locations P1-P9 as a function of the strengths and translational speeds of the mesoscale eddies. The speed of the cyclonically rotating winds at the inertial frequency is 13 m s$^{-1}$. Mesoscale eddies move westward. Different colors of lines represent different mesoscale eddy strengths.

## 5.5 Effect of Mesoscale Eddy Strengths

In addition to the effect of the eddy translational speed, other characteristics of mesoscale eddies such as the radius and strength of mesoscale eddies can also affect the energy exchange. Sixteen numerical experiments (denoted as ExpD1-16) are conducted in this section using various strengths of mesoscale eddies. In these sixteen experiments, the speed of cyclonically rotating winds at the inertial frequency is set to 13 m s$^{-1}$, the translational speed of mesoscale eddies is set to 8 cm s$^{-1}$, and the eddy translational direction to be westward. The $|SLA_c|$ values are set to 0.13 m, 0.26 m, 0.38 m, 0.51 m, 0.64 m, 0.77 m, 0.89 m, and 1.02 m for cyclonic and anticyclonic eddies, respectively.

Figure 9a shows that the sum of averaged speeds of the transferred NICs at nine locations as a function of the mesoscale eddy strengths for the cyclonic ($\sum \text{NICs\_U}_{CE}$) and anticyclonic eddies ($\sum \text{NICs\_U}_{CE}$). Both values of $\sum \text{NICs\_U}_{AE}$ and $\sum \text{NICs\_U}_{CE}$ are larger for higher eddy strengths, particularly for the anticyclonic eddies. For the $|SLA_c|$ values equal to 0.13 m, values of $\sum \text{NICs\_U}_{AE}$ and $\sum \text{NICs\_U}_{CE}$ are about 0.019 m s$^{-1}$ and about 0.003 m s$^{-1}$. The averaged speeds of

522   the converted NICs increase with the $|SLA_c|$ value, particularly for the anticyclonic eddies. For

523   $|SLA_c| = 1.02$ m, the averaged speeds of the transferred NICs are ~0.280 m s$^{-1}$ and ~0.175 m s$^{-1}$

524   for the anticyclonic and cyclonic eddies respectively, which are ~14.74 times and ~58.33 times

525   larger than the counterparts at $|SLA_c| = 0.13$ m. As the geostrophic strain field is relatively stronger

526   at the eddy edge, the average speeds of the converted NICs at the mesoscale eddy edge are larger

527   than that at the mesoscale eddy center.

528
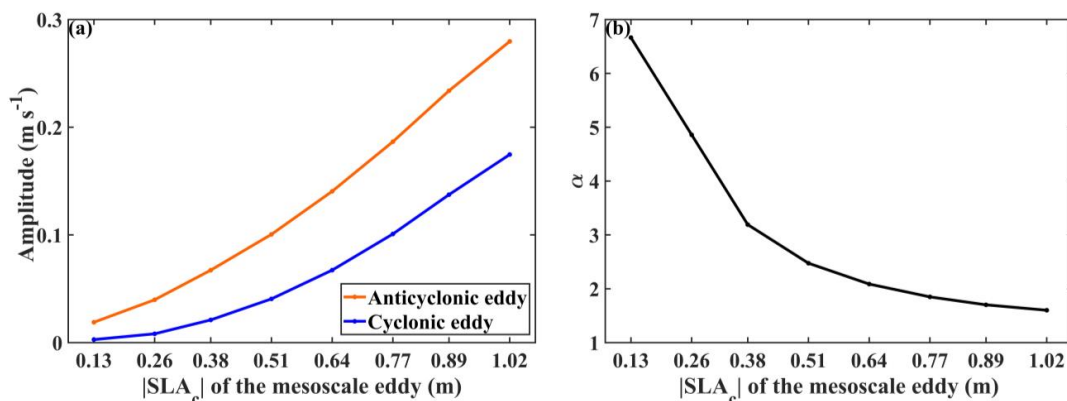


530   **Figure 9.** (a) Sum of averaged speeds of transferred NICs at 9 fixed locations P1-P9 as a function
531   of the strengths ($|SLA_c|$ of the mesoscale eddy) of the anticyclonic eddy (orange line) and cyclonic
532   eddy (blue line). (b) The $\alpha$ value as a function of the eddy strengths ($|SLA_c|$ of the mesoscale eddy).
533   The mesoscale eddy moves westward at the speed of 8 cm s$^{-1}$. The speed of the cyclonically
534   rotating wind speed at the inertial frequency is set to 13 m s$^{-1}$.

535

536   The $\alpha$ value also varies with the mesoscale eddy strength (Fig. 9b). The $\alpha$ value decreases

537   significantly from about 6.66 to 1.60 for the $|SLA_c|$ values in the range of 0.13 and 1.02 m. As

538   mentioned above, cyclonic eddies have limited ability in transferring their kinetic energy to NICs,

539   which differs significantly from anticyclonic eddies. However, stronger cyclonic eddies with more

540   eddy energy provide the more favorable condition for the energy transfer, which can narrow the

541   difference in the near-inertial energy transfer induced by anticyclonic eddies and cyclonic eddies.

542   Furthermore, stronger geostrophic currents lead to stronger geostrophic strain field which can

543   generate stronger NICs.

**5.6 Relative Vorticity and Strain**

As mentioned above, the anticyclonic eddies in the SML are more efficient than cyclonic eddies for transferring kinetic energy to NICs, which can be explained by the relative vorticity of the background flow ($\zeta$) defined in Eq. (1). In numerical experiments, the direction of the energy transfer is bidirectional, but primarily positive, that is, from mesoscale eddies to NICs. For cyclonic eddies, the direction of the energy transfer is from the NICs to the cyclonic eddy under cyclonically rotating winds at frequencies of $0.25f$, $0.75f$ and $1.25f$ and anticyclonically rotating winds at frequencies of $-1.1f$, $-0.9f$ and $-0.75f$. When the frequencies of anticyclonically rotating winds are range from $-1.5f$ to $-0.9f$, the energy transfer is also negative in the anticyclonic eddy. The $\alpha$ value is more than 1.0 for about 88% of these experiments, which indicates that the transferred near-inertial energy is larger in anticyclonic eddies than cyclonic eddies.

In addition to the relative vorticity and translational speed of a mesoscale eddy, the normal strain and shear strain of the background flow can also affect the energy transfer between the mesoscale eddy and NICs in the SML. Jing et al. (2017) proposed a method to calculate the rate of energy transfer from background mesoscale eddies to wind-induced NICs. Following Jing et al. (2017), the energy transfer rate ($\varepsilon$) between the NICs and the mesoscale eddy in the SML is given as

$$\varepsilon = -\rho H_{mix}\left(uuU_x + uvU_y + uvU_x + vvV_y\right), \qquad (25)$$

where $u$ and $v$ are respectively the zonal and meridional components of the near-inertial current velocity reproduced by the modified slab model, and subscripts $x$ and $y$ in $U$ and $V$ represent partial derivatives. The positive $\varepsilon$ mean the energy transfer from the mesoscale eddy to the NICs, and the negative $\varepsilon$ indicates the backward energy cascade. In the numerical experiments, the NICs can be generated directly by the cyclonic winds, and the wind-induced NICs can further interact with the mesoscale eddy and transfer the near-inertial energy from the mesoscale eddy to the NICs when the mesoscale eddy passed by the nine locations P1-P9. Therefore, we also calculate the energy transfer rate and Okubo-Weiss parameter at the nine fixed locations P1-P9 in the sensitivity experiments ExpA3, ExpC1-C9 and ExpD1-D16, which are under the same wind conditions.

When the Okubo-Weiss parameters are negative, the energy transfer rate decreases as the Okubo-Weiss parameter increases. However, when the Okubo-Weiss parameters are positive, the energy transfer rate shows an elevated trend with the increase of the Okubo-Weiss parameter (Fig.

574 10). Based on limited sensitivity studies, we found the relative vorticity and the strain of the

575 mesoscale eddy both have an influence on the near-inertial energy transferred by interactions

576 between mesoscale eddies and NICs.

577
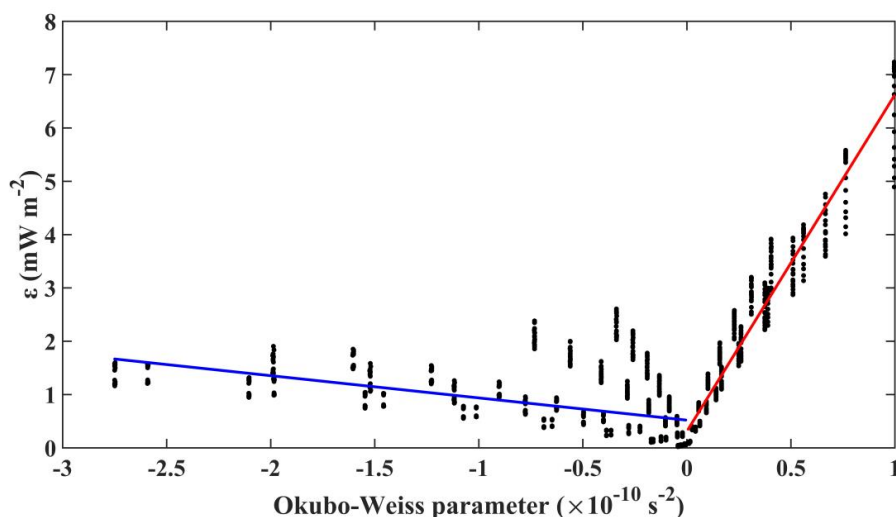


578

579 **Figure 10.** Scatterplot between the energy transfer rate and the Okubo-Weiss parameter. The blue
580 (red) line is the linear fitting line when the Okubo-Weiss parameters are negative (positive).

581 **6 Theoretical Analyses**

582 **6.1 Solutions in the Frequency Domain**

583 To gain better understanding of the role of the relative vorticity in the background flow for

584 anticyclonic eddies to be significantly more efficient than the cyclonic eddies in transferring their

585 kinetic energy to NICs, we examine analytically the effect of the relative vorticity in the frequency

586 domain solution of the modified slab model.

587 The modified slab model can be written in the tensor form:

588
$$\frac{\partial}{\partial t}\begin{Bmatrix} u \\ v \end{Bmatrix} + \begin{bmatrix} a_1 & b_1 \\ a_2 & b_2 \end{bmatrix}\begin{Bmatrix} u \\ v \end{Bmatrix} = \begin{Bmatrix} c_1 \\ c_2 \end{Bmatrix}, \tag{26}$$

589 where, $a_1 = U_x + r$, $a_2 = V_x + f$, $b_1 = U_y - f$, $b_2 = V_y + r$, $c_1 = \tau_x/\rho H_{mix}$ and $c_2 = \tau_y/$

590 $\rho H_{mix}$. For simplicity, we consider the steady wind forcing to eliminate the wind-induced NICs

25

591    here. In the case of steady winds, we use the Fourier transform to translate the modified slab model
592    from the time domain into the frequency domain:

$$\begin{bmatrix} a_1 + i\omega & b_1 \\ a_2 & b_2 + i\omega \end{bmatrix} \begin{Bmatrix} \tilde{u} \\ \tilde{v} \end{Bmatrix} = \begin{Bmatrix} \tilde{c_1} \\ \tilde{c_2} \end{Bmatrix}, \tag{27}$$

594    where $\omega$ is the frequency and variables with a tilde represent the values after Fourier transform.

595    Assuming the mesoscale eddy is in an almost steady state during an inertial period (Jing et al.
596    2017), the analytical solution for the zonal and meridional components of NICs in the frequency
597    domain can be written as

$$\tilde{u} = \frac{(b_2 + i\omega) \cdot 2 \cdot \pi \cdot c_1 \cdot \delta(\omega) - b_1 \cdot 2 \cdot \pi \cdot c_2 \cdot \delta(\omega)}{(a_1 + i\omega)(b_2 + i\omega) - a_2 b_1}, \tag{28}$$

$$\tilde{v} = \frac{(a_1 + i\omega) \cdot 2 \cdot \pi \cdot c_2 \cdot \delta(\omega) - a_2 \cdot 2 \cdot \pi \cdot c_1 \cdot \delta(\omega)}{(a_1 + i\omega)(b_2 + i\omega) - a_2 b_1}, \tag{29}$$

600    where $\delta(\omega)$ is the Dirac Delta function.

601    Based on Perceval's theorem, the energy of NICs is the same in both the time and frequency
602    domains:

$$\frac{1}{T} \int |U(t)|^2 dt = \int |U(\omega)|^2 d\omega, \tag{30}$$

604    where $T$ is the total period.

605    The time-mean near-inertial kinetic energy $\overline{U_{NIW_s}}^2$ in the time domain can be written as

$$\overline{U_{NIW_s}}^2 = \overline{u^2} + \overline{v^2}, \tag{31}$$

$$\overline{u^2} = \int \frac{((b_2 c_1 - b_1 c_2)^2 + \omega^2 c_1{}^2) \cdot ((2 \cdot \pi \cdot \delta(\omega))^2)}{(a_2 b_1 - a_1 b_2 + \omega^2)^2 + \omega^2 (a_1 + b_2)^2} \cdot d\omega, \tag{32}$$

$$\overline{v^2} = \int \frac{((a_1 c_2 - a_2 c_1)^2 + \omega^2 c_2{}^2) \cdot ((2 \cdot \pi \cdot \delta(\omega))^2)}{(a_2 b_1 - a_1 b_2 + \omega^2)^2 + \omega^2 (a_1 + b_2)^2} \cdot d\omega. \tag{33}$$

609    For a unidirectional laterally sheared geostrophic flow and the southwestward wind, U=0,
610    V=V(x), $c_1 < 0$ and $c_2 < 0$. Substitution of $a_1 = r$, $a_2 = \zeta + f$, $b_1 = -f$ and $b_2 = r$ into Eq.
611    (32) and Eq. (33) yields

$$\overline{u^2} = \int \frac{((rc_1 + fc_2)^2 + \omega^2 c_1{}^2)((2 \cdot \pi \cdot \delta(\omega))^2)}{(r^2 - \omega^2 + f(\zeta + f))^2 + 4\omega^2 r^2} d\omega, \tag{34}$$

$$\overline{v^2} = \int \frac{((rc_2 - (\zeta + f)c_1)^2 + \omega^2 c_2{}^2)((2 \cdot \pi \cdot \delta(\omega))^2)}{(r^2 - \omega^2 + f(\zeta + f))^2 + 4\omega^2 r^2} d\omega. \tag{35}$$

614    Since the relative vorticity is negative in anticyclonic eddies, the denominator term for $\overline{u^2}$ in
615    Eq. (34) is less than the value with the relative vorticity to be positive. Therefore, the value of $\overline{u^2}$
616    is greater in anticyclonic eddies than in cyclonic eddies. For the positive relative vorticity, the

617    numerator term of $\overline{v^2}$ is smaller and the denominator term in Eq. (35) becomes larger than the case

618    of negative vorticity. This indicates that $\overline{v^2}$ is more elevated in the anticyclonic eddies. Since both

619    $\overline{u^2}$ and $\overline{v^2}$ are elevated when the relative vorticity is negative than counterparts with the positive

620    relative vorticity, anticyclonic eddies can transfer more near-inertial energy than cyclonic eddies.

621    **6.2 Analytical Solution**

622    An analytical solution based on the modified slab model is considered here to demonstrate

623    that mesoscale eddies can transfer more near-inertial energy for stronger winds. The modified

624    slab model cane be written as

625
$$\frac{\partial u}{\partial t} + a_1 u + b_1 v = c_1, \tag{36}$$

626
$$\frac{\partial v}{\partial t} + a_2 u + b_2 v = c_2, \tag{37}$$

627    where, $a_1 = U_x + r$, $a_2 = V_x + f$, $b_1 = U_y - f$, $b_2 = V_y + r$, $c_1 = \tau_x / \rho H_{mix}$, $c_2 = \tau_y / \rho H_{mix}$,
628    $\tau_x = A cos ft$ and $\tau_y = A sin ft$.

629    For the cyclonic wind, substitution of Eq. (36) into Eq. (37) yields

630
$$\frac{\partial^2 u}{\partial t^2} + (a_1 + b_2)\frac{\partial u}{\partial t} + (a_1 b_2 - a_2 b_1)u = b_2 c_1 - (f + b_1)c_2 \tag{38}$$

631
$$\Delta = (a_1 + b_2)^2 - 4(a_1 b_2 - a_2 b_1). \tag{39}$$

632    The analytical solutions of the current to the modified slab model are

633
$$u_{Modified} = e^{\gamma t}(Q_1 cos\beta t + Q_2 sin\beta t) + Q_3 cos ft + Q_4 sin ft, \tag{40}$$

634
$$v_{Modified} = \frac{1}{b_1}(c_1 - e^{\gamma t}(a_1 + \gamma)(Q_1 cos\beta t + Q_2 sin\beta t)$$

635
$$-e^{\gamma t}\beta(Q_2 cos\beta t - Q_1 sin\beta t) + (fQ_3 - a_1 Q_4)sin ft - (fQ_4 + a_1 Q_3)cos ft), \tag{41}$$

636    where

637
$$\gamma = -\frac{a_1 + b_2}{2}, \tag{42}$$

638
$$\beta = \frac{\sqrt{-\Delta}}{2}, \tag{43}$$

639
$$Q_1 = -Q_3, \tag{44}$$

640
$$Q_2 = \frac{c_1 + \gamma Q_3 - fQ_4}{\beta}, \tag{45}$$

641
$$Q_3 = \frac{Ab_2(a_1 b_2 - a_2 b_1 - f^2) + A(f + b_1)(fa_1 + fb_2)}{\rho H_{mix}((a_1 b_2 - a_2 b_1 - f^2)^2 + (fa_1 + fb_2)^2)}, \tag{46}$$

642
$$Q_4 = \frac{\rho H_{mix} Q_3(fa_1 + fb_2) - A(f + b_1)}{\rho H_{mix}(a_1 b_2 - a_2 b_1 - f^2)}. \tag{47}$$

643  Increasing the wind stress $c_1$ and $c_2$ by a factor of $n$ named $c_1'$ and $c_2'$ yields

644
$$c_1' = nc_1 = \frac{n\tau_x}{\rho H_{mix}} = \frac{nA\cos ft}{\rho H_{mix}}, \tag{48}$$

645
$$c_2' = nc_2 = \frac{n\tau_y}{\rho H_{mix}} = \frac{nA\sin ft}{\rho H_{mix}}. \tag{49}$$

646  Substitution of $c_1'$ and $c_2'$ into $Q_3$ and $Q_4$ yields

647
$$Q_3' = \frac{nAb_2(a_1 b_2 - a_2 b_1 - f^2) + nA(f+b_1)(fa_1 + fb_2)}{\rho H_{mix}((a_1 b_2 - a_2 b_1 - f^2)^2 + (fa_1 + fb_2)^2)} = nQ_3, \tag{50}$$

648
$$Q_4' = \frac{\rho H_{mix} nQ_3(fa_1 + fb_2) - nA(f+b_1)}{\rho H_{mix}(a_1 b_2 - a_2 b_1 - f^2)} = nQ_4. \tag{51}$$

649  Substitution of $Q_3$ and $Q_4$ into $Q_1$ and $Q_2$ yields

650
$$Q_1' = -nQ_3 = nQ_1, \tag{52}$$

651
$$Q_2' = \frac{nc_1 + \gamma nQ_3 - fnQ_4}{\beta} = nQ_2. \tag{53}$$

652  Therefore, the current with the increased wind stress to the modified slab model is given as

653
$$u_{Modified}' = nu_{Modified}, \tag{54}$$

654
$$v_{Modified}' = nv_{Modified}. \tag{55}$$

655  The analytical solution of the current to the original slab model is

656
$$U_{Original} = \frac{Ae^{ift}}{\rho H_{mix}(if+r)} + \left( \left( \frac{Ae^{-(if+r)t}}{\rho H_{mix}(if+r)} \right) \left( \frac{if}{2if+r} \right) \left( 1 - e^{(2if+r)t} \right) \right) - \frac{Ae^{-(if+r)t}}{\rho H_{mix}(if+r)}. \tag{56}$$

657  Therefore, the current with the increased wind stress to the original slab model is given as

658
$$U_{Original}' = nU_{Original}. \tag{57}$$

659  The above analytical solutions demonstrate that when the wind stress increases by $n$ times,

660  the current speeds simulated by the modified and original slab models both increase by $n$ times.

661  The differences in the average speeds of NICs between the modified and original model represent

662  the transferred near-inertial energy by the interaction between mesoscale eddies and near-inertial

663  motions (Eq. (21) and (22)). As the NICs are the component of the total currents in the near-inertial

664  frequency band, the transferred near-inertial energy in the mesoscale eddies also increases by a

665  factor of n times when the wind stress is multiplied by n times. This feature is consistent with our

666  sensitivity experiments in Sect. 5.

667  **7 Summary and Discussion**

668  Analysis of in situ current observations at two offshore ADCP mooring sites in the northern

669  South China Sea (nSCS) demonstrated that relatively strong near-inertial currents (NICs) occurred

670   during certain periods of nearly steady winds in the lower part of the ocean surface mixed layer

671   (SML). The NICs produced by the original slab model are significantly larger than the observations,

672   indicating other important processes operating over the area. We followed Welle (1982) and Jing

673   et al. (2017) and used a modified slab model in this study by including contributions from the

674   background geostrophic currents. Using the surface geostrophic currents inferred from the satellite

675   sea level data and assuming the geostrophic currents in the SML is vertically uniform, we found

676   that the modified slab model performs significantly better than the original slab model in

677   reproducing the observed NICs at two ADCP mooring sites in the nSCS. Examinations of

678   observations and numerical results produced by the modified and original slab models revealed

679   the occurrence of the energy exchange between the mesoscale eddies and the NICs. Based on the

680   energy budget analysis for NICs during the observational period, the difference of the near-inertial

681   wind power input between the original slab model and the modified slab model is the same order

682   as the energy transfer rate (Eq. 25). This also indicates the importance of the near-inertial energy

683   transfer induced by the interaction between mesoscale eddies and NICs in the SML during the

684   observational period.

685       The modified slab model and original slab model were then used to examine sensitivity to

686   winds and eddy parameters with idealized mesoscale eddies under cyclonic winds. Both cyclonic

687   and anticyclonic mesoscale eddies were considered, using the universal eddy structure suggested

688   by Zhang et al. (2013). One of our major findings is that anticyclone eddies can transfer more

689   kinetic energy to NICs than cyclonic eddies. Idealized experiments show that induced NICs speed

690   in anticyclonic eddies can reach over 6 times the speed in cyclonic eddies. We also found that the

691   energy transfer rate is related to the Okubo-Weiss parameter. When the Okubo-Weiss parameter

692   is positive, the energy transfer rate is elevated with the larger Okubo-Weiss parameter.

693       Analyses of model results in 196 numerical experiments using the modified slab model

694   demonstrated that there exists bidirectional energy transfer between mesoscale eddies and NICs.

695   The direction of the energy transfer is primarily from mesoscale eddies to NICs. When the cyclonic

696   winds rotate at frequencies of $0.25f$, $0.75f$ and $1.25f$ and the anticyclonic winds rotate at

697   frequencies of $-1.1f$, $-0.9f$ and $-0.75f$, the direction of the energy transfer is negative in the

698   cyclonic eddy, that is, from NICs to cyclonic eddies. Under anticyclonically rotating winds at

699   frequencies of $-1.5f$, $-1.25f$, $-1.1f$ and $-0.9f$, the negative energy transfer also occurs in the

700   anticyclonic eddy. The NICs transferred from mesoscale eddies are stronger for higher wind

701    speeds, faster translational speeds and stronger strengths of mesoscale eddies. When the wind

702    stress increases by a factor of $n$ times, the amplitudes of the converted NICs are also multiplied by

703    $n$ times. The NICs transferred in mesoscale eddies by the interactions between mesoscale eddies

704    and NICs are stronger for higher translational speeds of anticyclonic eddies. At the translational

705    speeds of 11 cm s$^{-1}$, the ratios of the amplitudes of the converted NICs by anticyclonic eddies to

706    that transferred by cyclonic eddies reach maximum values.

707        For analytical considerations, the modified slab model was transferred from the time domain

708    to the frequency domain using the Fourier transform. Using Parseval's theorem, we derived the

709    time-mean value of the induced NICs. The analytical expression was used to demonstrate that, for

710    the negative relative vorticity, i.e., such as within an anticyclonic eddy, the transferred NICs are

711    larger in an anticyclonic eddy than a cyclonic eddy. The analytical solution under the cyclonic

712    winds also demonstrated that the NICs transferred by mesoscale eddies increase linearly with the

713    wind stress. These analytical results are consistent with the results produced by the modified and

714    original slab models.

715        We also conducted the same set of numerical experiments using steady winds in both constant

716    speeds and direction and model results in the steady winds are not presented here due to the page

717    limit. Our main findings on the energy transfer between mesoscale eddies and NICs in these

718    experiments with the steady winds are the same as the results using the rotating winds.

719        This study suggests that there is bidirectional energy transfer between mesoscale eddies and

720    NICs in the SML, of which the mechanism and influence factors are further explored by idealized

721    simulations. Our findings can further contribute to the understanding of the energy budget in the

722    global ocean and the ocean response to the climate change. In order to examine major physical

723    processes affecting the NICs generated by the mesoscale eddies and quantify their influence on

724    turbulent mixing in the deeper ocean, further studies are needed using a three-dimensional ocean

725    circulation model.

726    **Data availability**

727    All the data can be obtained by contacting the authors.

**Competing interests**

The authors declare that they have no conflict of interest.

**Acknowledgments**

**References**

Alford, M. H.: Improved global maps and 54-year history of wind-work on ocean inertial motions, Geophys. Res. Lett., 30(8), https://doi.org/10.1029/2002GL016614, 2003.

Alford, M. H., MacKinnon, J. A., & Simmons, H. L.: Near-inertial internal gravity waves in the ocean, Ann. Rev. Mar. Sci., 8, 95–123, https://doi.org/10.1146/annurev-marine-010814-015746, 2016.

Barkan, R., Srinivasan, K., & Yang, L.: Oceanic mesoscale eddy depletion catalyzed by internal waves, Geophys. Res. Lett., 48(18), e2021GL094376, https://doi.org/10.1002/essoar.10507068.1, 2021.

Boyer, T.P., O.K. Baranova, C. Coleman, H.E. Garcia, A. Grodsky, R.A. Locarnini, A.V. Mishonov, C.R. Paver, J.R. Reagan, D. Seidov, I.V. Smolyar, K.W. Weathers, & M.M. Zweng.: NOAA Atlas NESDIS 87, World Ocean Database 2018 [Dataset], https://www.ncei.noaa.gov/access/world-ocean-atlas-2018/, 2019.

Bühler, O., & McIntyre, M. E.: Wave capture and wave–vortex duality, J. Fluid Mech., 534, 67–95. https://doi.org/10.1017/S0022112005004374, 2005.

Chelton, D. B., Schlax, M. G., & Samelson, R. M.: Global observations of nonlinear mesoscale eddies, Prog. Oceanogr., 91(2), 167–216, https://doi.org/10.1016/j.pocean.2011.01.002, 2011.

Chen, S.: OSF, The Current Observation Data (S2 and S3) in the Mixed Layer [Dataset], https://doi.org/osf.io/r9kyz, 2023.

Chen, S., J. Polton, Hu, J., & Xing, J.: Local inertial oscillations in the surface ocean generated by time-varying winds, Ocean Dyn., 65, 1633–1641, https://doi.org/10.1007/s10236-015-0899-6, 2015a.

Chen, S., Hu, J. & J. A. Polton.: Features of near-inertial motions observed on the northern South China Sea shelf during the passage of two typhoons, Acta Oceanol. Sin., 34, 38–43, https://doi.org/10.1007/s13131-015-0594-y, 2015b.

Chen, S., J. A. Polton, Hu, J., & Xing, J.: Thermocline bulk shear analysis in the northern North Sea, Ocean Dyn., 66, 499–508, https://doi.org/10.1007/s10236-016-0933-3, 2016.

763  Chen, S., Chen, D. & Xing, J.: A study on some basic features of inertial oscillations and near-
764       inertial internal waves, Ocean Sci., 13, 829–836, https://doi.org/10.5194/os-2017-33, 2017.

765  Chen, G., Xue, H., & Wang, D.: Observed near-inertial kinetic energy in the northwestern South
766       China Sea, J. Geophys. Res.-Oceans, 118(10), 4965–4977, https://doi.org/10.5194/os-
767       2017-33, 2013.

768  Copernicus Climate Change Service, Climate Data Store.: Sea level gridded data from satellite
769       observations  for  the  global  ocean  from  1993  to  present  [Dataset],
770       https://doi.org/10.24381/cds.4c328c78, 2018.

771  D'Asaro E. A.: The energy flux from the wind to near-inertial motions in the surface mixed layer,
772       J.   Phys.   Oceanogr.,   15(8),   1043–1059,   https://doi.org/10.1175/1520-
773       0485(1985)015<1043:tefftw>2.0.co;2, 1985.

774  D'asaro, E. A., Eriksen C. C., & Levine M. D.: Upper-ocean inertial currents forced by a strong
775       storm. Part I: data and comparisons with linear theory, J. Phys. Oceanogr., 25(11), 2909–
776       2936, https://doi.org/10.1175/1520-0485(1995)025<2909:uoicfb>2.0.co;2, 1995.

777  Elipot, S., Lumpkin, R., & Prieto, G.: Modification of inertial oscillations by the mesoscale eddy
778       field, J. Geophys. Res.-Oceans, 115(C9), https://doi.org/10.1029/2009jc005679, 2010.

779  Ferrari, R., & Wunsch, C.: Ocean circulation kinetic energy: Reservoirs, sources, and sinks, Annu.
780       Rev. Fluid Mech., 41, 253–282, https://doi.org/10.1146/annurev.fluid.40.111406.102139,
781       2009.

782  Ford, R., McIntyre, M. E., & Norton, W. A.: Balance and the slow quasimanifold: some explicit
783       results,   J.   Atmos.   Sci.,   57(9),   1236–1254,   https://doi.org/10.1175/1520-
784       0469(2000)057<1236:BATSQS>2.0.CO;2, 2000.

785  Garrett, C.: What is the ''near-inertial'' band and why is it different from the rest of the internal
786       wave spectrum?, J. Phys. Oceanogr., 31, 962–971, https://doi.org/10.1175/1520-
787       0485(2001)031,0962: WITNIB.2.0.CO;2, 2001.

788  Gill A.: On the Behavior of Internal Waves in the Wakes of Storms, J. Phys. Oceanogr., 14(7),
789       1129–1151, https://doi.org/10.1175/1520-0485(1984)014<1129:otboiw>2.0.co;2, 1984.

790  Greatbatch, R. J.: On the response of the ocean to a travelling storm: Parameters and scales, J.
791       Phys.   Oceanogr.,   14,   59–78,   https://doi.org/10.1175/1520-
792       0485(1984)014,0059:OTROTO.2.0.CO;2, 1984.

793  Hersbach, H., Bell, B., Berrisford, P., Biavati, G., Horányi, A., Muñoz Sabater, J., Nicolas, J.,
794       Peubey, C., Radu, R., Rozum, I., Schepers, D., Simmons, A., Soci, C., Dee, D., & Thépaut,
795       J-N.: Copernicus Climate Change Service (C3S) Climate Data Store (CDS), ERA5 hourly
796       data  on  single  levels  from  1940  to  present  [Dataset],
797       https://doi.org/10.24381/cds.adbb2d47, 2023.

798  Jaimes, B., & Shay, LK.: Near-Inertial Wave Wake of Hurricanes Katrina and Ritaover Mesoscale
799       Oceanic   Eddies,   J.   Phys.   Oceanogr.,   40(6),   1320–1337,
800       https://doi.org/10.1175/2010JPO4309.1, 2010.

801  Jing, Z., Wu, L., & Ma, X.: Sensitivity of near-inertial internal waves to spatial interpolations of
802       wind stress in ocean generation circulation models, Ocean Modell., 99, 15–21,
803       https://doi.org/10.1016/j.ocemod.2015.12.006, 2016.

804  Jing, Z., Wu, L., & Ma, X.: Energy exchange between the mesoscale oceanic eddies and wind-
805      forced near-inertial oscillations, J. Phys. Oceanogr., 47(3), 721–733,
806      https://doi.org/10.1175/JPO-D-16-0214.1, 2017.

807  Jing, Z., Chang, P., DiMarco, S.F., & Wu, L.: Observed energy exchange between low-frequency
808      flows and internal waves in the Gulf of Mexico, J. Phys. Oceanogr., 48, 995–1008,
809      https://doi.org/10.1175/JPO-D-17-0263.1, 2018.

810  Jochum, M., Briegleb, B., Danabasoglu, G., Large., W, Norton, N., Jayne, S., Alford, M., & Bryan,
811      F.: The impact of oceanic near-inertial waves on climate, J. Clim., 26, 2833–2844,
812      https://doi.org/10.1175/JCLI-D-12-00181.1, 2013.

813  Kunze, E.: Near-inertial wave propagation in geostrophic shear, J. Phys. Oceanogr., 15(5), 544–
814      565, https://doi.org/10.1175/1520-0485(1985)015<0544:NIWPIG>2.0.CO;2, 1985.

815  Liu, G., Chen, Z., Lu, H., Liu, Z., Zhang, Q., He, Q., He, Y., Xu, J., Gong, Y., & Cai, S.: Energy
816      transfer between mesoscale eddies and near-inertial waves from surface drifter
817      observations, Geophys. Res. Lett., 50, e2023GL104729,
818      https://doi.org/10.1029/2023GL104729, 2023.

819  McWilliams, J. C.: Submesoscale currents in the ocean, Proc. R. Soc. A., 472(2189), 20160117,
820      https://doi.org/10.1098/rspa.2016.0117, 2016.

821  Mooers, C. N.: Several effects of a baroclinic current on the cross-stream propagation of inertial-
822      internal waves, Geophys. Fluid Dyn., 6(3), 245–275,
823      https://doi.org/10.1080/03091927509365797, 1975.

824  Muller, P.: On the diffusion of momentum and mass by internal gravity waves, J. Fluid Mech.,
825      77(4), 789–823, https://doi.org/10.1017/S0022112076002899, 1976.

826  Munk, W., & Wunsch, C.: Abyssal recipes II: Energetics of tidal and wind mixing, Deep-Sea Res.
827      Pt. I, 45, 1977–2010, https://doi.org/10.1016/S0967-0637(98)00070-3, 1998.

828  Noh, S., & Nam, S.: Observations of enhanced internal waves in an area of strong mesoscale
829      variability in the southwestern East Sea (Japan Sea), Sci. Rep., 10, 9068,
830      https://doi.org/10.1038/s41598-020-65751-1, 2020.

831  Oey, L. Y., Ezer, T., &Wang, D. P.: Loop current warming by hurricane Wilma, Geophys. Res.
832      Lett., 33(8), L08613, https://doi.org/ 10.1029/2006GL025873, 2006.

833  Okubo, A.: Horizontal dispersion of floatable particles in the vicinity of velocity singularities such
834      as convergences, Deep. Sea Res. Oceanogr. Abstr., 17(3), 445–454,
835      https://doi.org/10.1016/0011-7471(70)90059-8, 1970.

836  Paduan, J. D., Szoeke, R. A., & Weller, R. A.: Inertial oscillations in the upper ocean during the
837      Mixed Layer Dynamics Experiment (MILDEX), J. Geophys. Res., 94, 4835–4842,
838      https://doi.org/10.1029/JC094iC04p04835, 1989.

839  Perkins, H.: Observed effect of an eddy on inertial oscillations, Deep. Sea Res. Oceanogr. Abstr.,
840      23(11), 1037–1042, https://doi.org/10.1016/0011-7471(76)90879-2, 1976.

841  Pollard, R. T., & Millard, R. C.: Comparison between observed and simulated wind-generated
842      inertial oscillations, Deep. Sea Res. Oceanogr. Abstr., 17, 813–816,
843      https://doi.org/10.1016/0011-7471(70)90043-4, 1970.

844  Price, J. F., Weller, R. A., & Pinkel, R.: Diurnal cycling: Observations and models of the upper
845      ocean response to diurnal heating, cooling, and wind mixing, J. Geophys. Res., 91, 8411–
846      8427, https://doi.org/10.1029/JC091iC07p08411, 1986.

847    Sun, Z., Hu, J., & Zheng, Q.: Strong near-inertial oscillations in geostrophic shear in the northern
848        South China Sea, J. Oceanogr., 67(4), 377–384, https://doi.org/ 10.1007/s10872-011-0038-
849        z, 2011.

850    Thomas, L. N.: On the effects of frontogenetic strain on symmetric instability and inertia–gravity
851        waves, J. Fluid Mech., 711, 620–640, https://doi.org/ 10.1017/jfm.2012.416, 2012.

852    Thomas, L. N.: On the modifications of near-inertial waves at fronts: Implications for energy
853        transfer across scales, Ocean Dyn., 67(10), 1–16, https://doi.org/10.1007/s10236-017-
854        1088-6, 2017.

855    van Meurs, P.: Interactions between near-inertial mixed layer currents and the mesoscale: the
856        importance of spatial variabilities in the vorticity field, J. Phys. Oceanogr., 28(7), 1363–
857        1388, https://doi.org/10.1175/1520-0485(1998)0282.0.CO;2, 1998.

858    Vanneste, J.: Balance and spontaneous wave generation in geophysical flows, Annu. Rev. Fluid
859        Mech., 45, 147–172, https://doi.org/10.1146/annurev-fluid-011212-140730, 2013.

860    Wang, Y., Guan, S., Zhang, Z., Zhou, C., Xu, X., Guo, C., Zhao, W. & Tian, J.: Observations of
861        Parametric Subharmonic Instability of Diurnal Internal Tides in the Northwest Pacific, J.
862        Phys. Oceanogr., 54(3), 849-870, https://doi.org/10.1175/JPO-D-23-0055.1, 2024.

863    Weller, R. A.: The relation of near-inertial motions observed in the mixed layer during the JASIN
864        (1978) experiment to the local wind stress and to the quasi-geostrophic flow field, J. Phys.
865        Oceanogr., 12, 1122–1136, https://doi.org/10.1175/1520-0485(1982)0122.0.CO;2, 1982.

866    Wei, Z., Xue, H., & Qin, H.: Using idealized numerical experiment to study an eddy colliding with
867        an island, J. Trop. Oceanogr., 36(4), 35-47, https://doi.org/10.11978/2016118, 2017.

868    Whalen, C. B., Lavergne, C. D., Garabato, A. C. N., Klymak, J. M., & Sheen, K. L.: Internal wave-
869        driven mixing: Governing processes and consequences for climate, Nat Rev Earth Environ,
870        1(11), 606–621, https://doi.org/10.1038/s43017-020-0097-z, 2020.

871    Whitt, D. B., & L. N. Thomas.: Resonant generation and energetics of wind-forced near-inertial
872        motions in a geostrophic flow, J. Phys. Oceanogr., 45, 181–208,
873        https://doi.org/10.1175/JPO-D-14-0168.1, 2015.

874    Wunsch, C., & Ferrari, R.: Vertical mixing, energy and the general circulation of the oceans, Annu.
875        Rev. Fluid Mech., 36, 281–314, https://doi.org/10.1146/annurev.fluid.36.050802.122121,
876        2004.

877    Xie, J., & Vanneste, J.: A generalised-Lagrangian-mean model of the interactions between near-
878        inertial waves and mean flow, J. Fluid Mech., 774, 143–169,
879        https://doi.org/10.1017/jfm.2015.251, 2015.

880    Young, W. R., & Jelloul, M. B.: Propagation of near-inertial oscillations through a geostrophic
881        flow, J. Mar. Res., 55(4), 735–766, https://doi.org/10.1357/0022240973224283, 1997.

882    Zhai, X., Greatbatch, R. & Zhao, J.: Enhanced vertical propagation of storm-induced near-inertial
883        energy in an eddying ocean channel, Geophys. Res. Lett., 32(18), L18602,
884        https://doi.org/10.1029/2005GL023643, 2005.

885    Zhai, X., Greatbatch, R. J. & Eden, C.: Spreading of near-inertial energy in a 1/12° model of the
886        North Atlantic Ocean, Geophys. Res. Lett., 34(10), 421–428,
887        https://doi.org/10.1029/2007GL029895, 2007.

888    Zhang, Z., Zhang, Y., & Wang, W.: Universal structure of mesoscale eddies in the ocean, Geophys.
889        Res. Lett., 40(14), 3677–3681, https://doi.org/10.1002/grl.50736, 2013.